A Correlation Between Surface Densities of Young Stellar Objects and Gas in Eight Nearby Molecular Clouds

R. A. Gutermuth[1,2], J. L. Pipher[3], S. T. Megeath[4], P. C. Myers[5], L. E. Allen[6], & T. S. Allen[4]

ABSTRACT

We report the discovery and characterization of a power law correlation between the local surface densities of Spitzer-identified, dusty young stellar objects and the column density of gas (as traced by near-IR extinction) in eight molecular clouds within 1 kpc and with 100 or more known YSOs. This correlation, which appears in data smoothed over size scales of $\sim$1 pc, varies in quality from cloud to cloud; those clouds with tight correlations, MonR2 and Ophiuchus, are fit with power laws of slope 2.67 and 1.87, respectively. The spread in the correlation is attributed primarily to local gas disruption by stars that formed there or to the presence of very young sub-regions at the onset of star formation. We explore the ratio of the number of Class II to Class I sources, a proxy for the star formation age of a region, as a function of gas column density; this analysis reveals a declining Class II to Class I ratio with increasing column density. We show that the observed star-gas correlation is consistent with a star formation law where the star formation rate per area varies with the gas column density squared. We also propose a simple picture of thermal fragmentation of dense gas in an isothermal, self-gravitating layer as an explanation for the power law. Finally, we briefly compare the star gas correlation and its implied star formation law with other recent proposed of star formation laws at similar and larger size scales from nearby star forming regions.

Subject headings: dust, extinction – infrared: stars – stars: formation

1. Introduction

It has been long recognized that the density of young stars varies by orders of magnitude between different star forming regions. Herbig (1962) compared the low density of young stars in the Taurus star forming region to the high density of young stars in the Orion nebula and speculated

that these may form an evolutionary sequence, with the low density regions collapsing into denser structures. More recently, ground-based near-IR surveys of molecular clouds (e.g. Lada et al. 1991; Strom, Strom, & Merrill 1993; Carpenter 2000; Porras et al. 2003; Lada & Lada 2003) identified embedded dense young stellar clusters and groups in molecular clouds as well as a more diffuse population of low mass stars, showing that molecular clouds contain both a dense "clustered" and a diffuse "distributed" population. Although clusters could easily be identified in these surveys by searching for peaks in the surface density of sources, measurements of the number of distributed young stars in the clouds were dominated by uncertainties in the amount of contamination by field stars and the treatment of variable extinction through each cloud (Carpenter 2000). This led to a number of questions regarding the

[1]Five College Astronomy Dept., Smith College, Northampton, MA 01063

[2]Dept. of Astronomy, University of Massachusetts, Amherst, MA

[3]Dept. of Physics & Astronomy, University of Rochester, Rochester, NY

[4]Dept. of Physics & Astronomy, University of Toledo, Toledo, OH

[5]Harvard-Smithsonian Center for Astrophysics, Cambridge, MA

[6]National Optical Astronomy Observatories, Tucson, AZ

number and origin of young low mass stars outside of clusters (Lada et al. 1991; Li et al. 1997; Carpenter 2000). What fraction of the cloud population is found outside of clusters? Are they born in clusters and dynamically ejected to their observed positions (Evans et al. 2009)? Alternatively, if they are formed near their current positions, why do molecular clouds exhibit large variations in the density of young stars? Are the variations in density related to variations in the Jeans length within clouds (Teixeira et al. 2006; Gutermuth et al. 2009)? Better observational characterization of the relationship between the spatial distribution of YSOs and their natal cloud material is needed to understand the nature of the distributed component, constrain models of star formation in molecular clouds, and ascertain the underlying physics that determine the density and rate of star formation (e.g. Bate & Bonnell 2005; Krumholz & Tan 2007; Myers 2009a).

Sensitive *Spitzer* mid-IR and 24 μm surveys of nearby young clusters embedded in molecular clouds have enabled complete characterization of the full range of stellar densities in a range of star foming environments (e.g. Allen et al. 2007; Evans et al. 2009). Young stellar objects (YSOs) in the clouds are identified by the presence of IR-excess emission from circumstellar disks and/or envelopes. Several groups have developed methods to use *Spitzer*-determined YSO spectral energy distributions to characterize the sources as protostars (Class 0, I, or flat-spectrum) or pre-main sequence stars with disks (Class II or transition disks) (e.g. Gutermuth et al. 2009; Evans et al. 2009; Rebull et al. 2010). By employing strategies to minimize the contamination by background galaxies with similar infrared colors (e.g. Harvey et al. 2006; Gutermuth et al. 2008, 2009; Evans et al. 2009), the *Spitzer* surveys have yielded reliable, high spatial dynamic range distributions of YSOs in their natal clouds. These observations show that the clusters are peaks of a more extended population of young stars which tend to follow the morphology of the filamentary molecular clouds (Allen et al. 2007; Gutermuth et al. 2009; Evans et al. 2009). Thus, low density star forming regions are not limited to Taurus-like regions, but are also found in molecular clouds forming large clusters and high mass stars (Allen et al. 2007).

The wide range in observed YSO surface densities provides an opportunity to study how the density of young stars varies with the observed star formation efficiency and the properties of the co-spatial molecular gas. Recent work indicates that the star formation efficiency increases with the stellar density. Evans et al. (2009) showed that higher surface density YSO clusterings tend to exhibit higher star formation efficiency (30%) than lower density surroundings (3-6%). In a *Spitzer* survey of YSOs in the W5 molecular cloud, where a recent generation of star formation is proceeding on the peripheries of the evacuated cavities of adjacent HII regions, Koenig et al. (2008) found star-formation efficiencies of >10-17% for high surface density clusterings and 3% for lower density distributed regions, respectively. The fraction of *Spitzer* identified YSOs outside of clusters depends strongly on the adopted functional definition of stellar cluster, as there is no strong distinction in source spacings evident in the nearby YSO spacing data to suggest distinct "clustered" and "distributed" star-forming modes (Bressert et al. 2010). The continuous nature of the overall YSO surface density distribution in nearby clouds motivates a different approach whereby the local surface density of YSOs and the local column density of gas are compared. This approach does not require a functional definition of clustered or distributed star formation.

A similar approach has been used with success in observations of external galaxies. Kennicutt et al. (1998) outlines previously published results concerning the validity of the Schmidt Law of star formation in external galaxies, namely $\Sigma_{SFR} = A\Sigma_{gas}^N$, where the Σs refer to the observed surface densities of star formation rate and gas respectively (Schmidt 1959). For a limited range of densities and galaxy types these studies found N to be between 1 and 2. Kennicutt et al. (1998), using Hα emission as the star formation tracer, and CO and HI as the gas tracers for spiral galaxies, and Brγ emission and FIR dust emission as star and gas tracers respectively for infrared-selected starburst galaxies, show $N = 1.45 \pm 0.15$. Note that these observations measure the integrated star formation (as traced by recently formed OB stars) across multiple molecular clouds, hence the extragalactic laws should not be expected to apply directly to studies of low mass stars within

individual molecular clouds in our galaxy. That stated, Evans et al. (2009) compare Σ_{SFR} against Σ_{gas} for the seven nearby clouds surveyed by the *Spitzer* c2d Legacy survey against the Kennicutt-Schmidt Law, and find Σ_{SFR} to be $\sim$20 times larger than predicted by the law for the measured Σ_{gas}.

In this contribution, we perform a direct comparison between locally determined mass surface densities of YSOs and gas. This technique reveals a power law correlation between the YSO surface density and the gas surface density in all clouds, which we refer to hereafter as the star-gas correlation. Furthermore, using the ratio of protostars to pre-main sequence stars as an evolutionary indicatory, deviations from that correlation can be interpreted as regions of more or less time evolution in the star-gas correlation. We interpret these by adopting a star formation law of power law form and calculating the integral of the star formation rate over time vs. the remaining gas density. We present a simple analysis which shows that the higher density regions of a cloud produce stars which consume their local gas more rapidly, and the relation between log Σ_* vs. log Σ_{gas} increasingly deviates from a power law with time, particularly at high gas densities. Nevertheless, the observed correlation can be reasonably well explained by an underlying $\Sigma_{SFR} = A\Sigma_{gas}^2$ star formation law. We examine the observed deviations from the correlation and argue that they result from a combination of gas dispersion in rich clusters and non-coevality within the molecular clouds.

In Section 2, we summarize the *Spitzer* YSO lists compiled from prior observations, as well as the near-IR extinction maps (as a tracer for the molecular gas surface density). In Section 3, we demonstrate and characterize the observed correlations. In Section 4, we present some analysis of the correlation and its implications including: a simple evolutionary model to demonstrate the robustness of an underlying star formation law of power law form under the effects of early gas depletion; a simple thermal fragmentation model that predicts the central values of the ranges of power law index and normalizations observed; a brief comparison to the Schmidt-Kennicutt star formation law for galaxies. Finally, we summarize our findings in Section 5.

2. Data and Methodology

Numerous surveys of nearby star formation regions have been performed using *Spitzer* (e.g. Gutermuth et al. 2004; Megeath et al. 2004; Jørgensen et al. 2006; Harvey et al. 2007; Allen et al. 2007). One of the most useful products of these observations is a largely flux-limited census of high probability young stellar object candidates as indicated by their excess mid-infrared emission relative to a photospheric spectral energy distribution. *Spitzer* data cannot be used to uniquely distinguish diskless pre-main-sequence stars from field stars, but this limitation to the total YSO census is relatively minor for young, embedded star forming regions where few members have had sufficient time for their disks to disperse (10-50% for ages <1 to 3 Myr; Hernández et al. 2008).

Table 1 lists the cloud surveys we have used for this analysis, the references for these surveys, and some general statistics for each. We selected large clouds with 100 YSO members or more, with a known range of YSO surface densities that is greater than one order of magnitude, and located within 1 kpc of the Sun, as these typically are complete for infrared-excess sources down to roughly 0.2 $M_\odot$ at an age of 1 Myr (Baraffe et al. 1998), and to even lower masses (< 0.08 $M_\odot$) for the closer clouds. However, the presence of bright sources as well as bright, structured nebulosity near the centers of some clusters does significantly reduce the completeness relative to regions of lower YSO density. The most significant example of this issue is the Trapezium area of Orion, where Megeath et al. (in prep.) have performed a detailed comparison between the *Spitzer* and *Chandra* source lists to examine the issue of incompleteness. The completeness decreases rapidly in the inner regions of the Orion nebula: the comparison has revealed that the Spitzer survey may identify 50% of the dusty YSOs averaged over the inner 0.5 parsec radius, and only identify 30% of the YSOs in the inner 0.2 pc. Other expected trouble spots include the centers of the MonR2 and GGD 12-15 clusters in the MonR2 cloud, and the center of the Cep A cluster in the CepOB3 cloud. In these regions of generally high YSO surface density, we are likely underestimating the true surface density of YSOs.

The adopted datasets are relatively uniform

in their observing parameters, but heterogeneous in their data treatment, including different software pipelines used for mosaic construction, source extraction algorithms, photometric measurement techniques, and finally source classification schemes. While the results from the first three items are expected to be similar, it is not intuitive to ascertain the degree of equivalence of the YSO type classification schemes. Some investigations into this issue have suggested that the relative numbers of Class I and II YSOs are found to vary at the 10% level by technique (Allen et al. 2007; Rebull et al. 2010; Gutermuth et al. 2009); method dependent variation at that level should not strongly affect the results presented here.

2.1. Large-scale Near-IR Extinction Mapping

To characterize the spatial distribution of gas column density in the target molecular clouds, we have adopted dust column density maps from the near-IR reddening of stars in the field of view, assuming that the dust and gas column densities are proportional. The maps are constructed following the method described by Gutermuth et al. (2009) for the Orion A and B, MonR2, CepOB3, S140, and North America Nebula (NANeb hereafter) clouds. For the c2d survey clouds presented (Ophiuchus, Perseus, and Serpens), the extinction maps delivered as part of that survey's enhanced data products have been adopted, after a comparison between overlapping regions of the c2d maps and the maps of Gutermuth et al. (2009) showed consistent results (see Appendix A). The former set of maps were generated at the Nyquist sampling resolution for the median $n = 20$ nearest neighbor distance in each region. The sampling resolutions of each map are tabulated in Table 1, though it is worth noting that the effective resolution of these maps decays somewhat at higher column density. The mean and maximum values after baseline subtraction, and the value subtracted as a baseline, are also included in the table. The empirical extinction law of Rieke & Lebofsky (1985) was adopted to convert the $H - K_S$ color excesses to A_V ($A_V/E\{H - K_S\} = 15.9$). The gas column density maps are computed from the extinction maps by assuming a constant gas to dust ratio of $A_V/N(H_2) = 10^{-21}$ magnitudes-cm^2. This ratio has been observed to vary by up to a factor of two

(e.g. Winston et al. 2010), however, such variation will have a modest effect on the star-gas correlation which is observed over more than an order of magnitude range in the gas column density.

2.2. YSO Surface Density Estimation

We have performed a nth nearest neighbor surface density analysis of the *Spitzer*-identified YSO distribution in each cloud, similar to the analysis employed in Gutermuth et al. (2009). For these values, n was set to 11 - this value results in uncertainties of 33% in the surface density estimation (Casertano & Hut 1985). We first obtained these nearest neighbors centered on each of the identified YSOs; for a sample of q YSOs this would result in q surface density measurements centered on the YSOs. We also obtained nearest neighbor distances for a uniform rectangular grid of points in RA and Dec; this is the same procedure used to generate nearest neighbor density maps in several recent papers (e.g. Gutermuth et al. 2005; Román-Zúñiga et al. 2008; Chavarría et al. 2008; Jørgensen et al. 2008; Gutermuth et al. 2008; Evans et al. 2009; Gutermuth et al. 2009). To facilitate comparisons between the stellar density and the gas column density, the grid vertices we have adopted here are identical to the extinction map's pixel positions for each region. The combined analysis yields two surveys of the gas and stellar surface densities, one that follows the YSO spatial distribution and the other that is unbiased and spatially regular. In both cases, the resulting densities of YSOs per solid angle in the sky are converted to mass per square parsec using the distances in Table 1 and adopting an average stellar mass of 0.5 $M_\odot$.

3. An Observed Correlation in the Surface Density of YSOs and Dust

Visual comparisons between the distribution of *Spitzer*-identified YSOs relative to maps of gas structure in their natal molecular clouds have shown that there is considerable similarity between them (e.g. Megeath et al. 2004; Allen et al. 2007; Evans et al. 2009; Gutermuth et al. 2009). In Figure 1, we show one of the best examples of cloud-YSO correlation, the MonR2 cloud. The red dots are the positions of *Spitzer*-identified YSOs, the grayscale image is the 2MASS-derived extinc-

tion map, and the green line outlines the *Spitzer* mid-IR survey coverage. The YSOs appear to congregate in the regions of detectable extinction, peaking in density at or near the positions of highest extinction. Figure 2 is the same figure, but for the CepOB3 cloud. Here, the apparent correlation is similar if one considers only the regions of significant extinction. However, there is an exposed young cluster, CepOB3b, in the northwest corner of the coverage where there are many YSOs present and very little local extinction; the gas in this region has likely been dispersed by winds and radiation from associated high mass stars. (See Figures 3-8 for similar figures for the rest of the clouds.)

To quantify the apparent correlation, we plot (on a log-log scale) the YSO mass surface density Σ_* vs. the molecular gas mass column density Σ_{gas} for MonR2, CepOB3, and six other star-forming clouds in Figures 9 & 10, utilizing the data and conversion factors described above. In Fig. 9 for YSO-centered sampling, red points represent central YSOs classified as protostars (hereafter Class I, though Class 0 and flat spectrum sources are included), and grey points represent those that are classified as pre-main sequence stars with disks (hereafter Class II, though transition disks are included). The black hatched regions represent regions in the plot space where the extinction is too low to be reliably measured in the near-IR at these resolutions (specifically $A_V < 1$) and where the surface density of stars is consistent with residual contamination from AGN (7 deg^{-2}; Gutermuth et al. 2009)[1]. The bias toward sampling only in positions with YSOs is addressed in Fig. 10. Here, plot points are sampled uniformly by position on the grid defined by the extinction map sampling, yielding an area-sampled, rather than YSO-sampled, view of the correlation.

Regardless of the view used, every cloud examined exhibits a positive power law trend in the surface density of stars and column density of gas. The MonR2 and Ophiuchus clouds stand out as having particularly cohesive loci relating these surface densities (Pearson coefficients of the log-log data are 0.87 and 0.83, respectively), thus we use

their correlation data to characterize the trend in detail. Using the same fitting method used by Flaherty et al. (2007)[2], we fit lines to the log Σ_* vs log Σ_{gas} data for MonR2 and Ophiuchus, finding them well fit with power law indexes of 2.67 ± 0.02 and 1.87 ± 0.03, respectively. Uncertainties in these values are simply the intrinsic slope uncertainty from the fit; we estimate a systematic uncertainty of < 0.04 based on a comparative analysis of Ophiuchus using both our extinction mapping technique, and that of c2d (see Appendix A). The fits are overlaid as polygons (green/steeper and blue/shallower for MonR2 and Ophiuchus, respectively) on the measurements for all clouds in Figs. 9 & 10 to demonstrate that the correlations for the other clouds are largely consistent with a power law of index $\sim$2. However, most clouds have some larger spread in the observed correlation relative to MonR2 and Ophiuchus ($\sim$1 dex spread), and this fact deserves closer examination. We have included fit results for all of the clouds in Table 2, for reference.

The more complex relationships seen in the other clouds appear related to evolutionary differences in the star-gas correlation among different structures within these clouds. For example, the main cluster core of the IC 348 region is well known to be a more evolved population of YSOs, with evolved disks (e.g. Muench et al. 2007), a low disk fraction (e.g. Lada et al. 2006), a high ratio (27) of Class II to Class I sources (e.g. Gutermuth et al. 2009), and low mean extinction relative to other young clusters (e.g. Jørgensen et al. 2008; Gutermuth et al. 2009). All of these observations indicate an evolved YSO population and thus significant time for the YSOs and the intermediate mass central members to have dispersed the local gas via feedback processes. In the YSO vs. gas surface densities diagram for Perseus, the subset of points that are significantly over-dense in stars relative to the gas density predominantly belong to the IC 348 exposed cluster core. Perseus also has several regions that are under-dense in stars relative to gas. These regions are typically located in the

---

[1]This value is higher than the value reported for c2d (e.g. Harvey et al. 2007), but we apply it across all clouds for consistency in treatment.

[2]The Flaherty et al. (2007) algorithm is an IDL implementation of χ^2 minimization of the two dimensional perpendicular offsets from a line fit, thereby implicitly incorporating uncertainty in both axis quantitites, following the analysis of Press et al. (1992).

well-studied dark clouds in Perseus, such as B5 and L1448, where the YSOs in these objects are predominantly confirmed Class 0 and Class I objects (Jørgensen et al. 2008; Enoch et al. 2008) with very few more evolved Class II sources. This indicates relative youth when compared to more typical embedded clusters like NGC 1333, which has a more standard ratio of Class II to Class I sources (3.7; Gutermuth et al. 2009). Ultimately, this study reveals that the Perseus cloud is an outlier relative to other nearby molecular clouds because of its heterogeneous composition of evolutionary states among its star-forming sites.

The Cep OB3 giant molecular cloud (GMC) appears to be a simpler (yet more numerous in YSOs) analogue of Perseus in that it has a subset of YSOs that deviate from the observed trend, namely the large, exposed Cep OB3b cluster consisting of two sub-clusters, Cep OB3b-east and Cep OB3b-west (Allen et al. in prep.). Cep OB3b-east has an abnormally large current star-formation efficiency (80%; Getman et al. 2009). The cluster is found to be adjacent to two massive molecular clumps indicating that most of the natal gas has been dispersed (Getman et al. 2009; Allen et al. in prep.). Interestingly, the similarity of heterogeneous evolutionary states in CepOB3 and Perseus may continue into the very young regime as well; there are some regions in the Cep OB3 molecular cloud which are overdense in gas relative to YSOs hinted at in the area-sampled analysis shown in Fig. 10.

Given these qualitative regional evolutionary differences, we investigate the degree that YSO evolution may trace differences in the Σ_* vs. Σ_{gas} analysis. We visualize the differing Class II to Class I ratios (N_{II}/N_I) of regions above or below the power law trend by assuming that the power law index is always 2 and computing the implied offset coefficient for the power law for each YSO individually. These values, Σ_*/Σ_{gas}^2, then may be composed into histograms separated by YSO evolutionary class. We have produced such histograms for all of the clouds considered here (see Figure 11). The black histograms are the Class II YSO values, and the red histograms are the same, but for the Class I YSOs scaled up by 3.7, the median ratio of Class II to Class I sources in nearby clusters (Gutermuth et al. 2009). Both have been normalized to the peak value among both histograms. The green histogram plots the Class II YSO data, but now scaled to the Class I data's normalization and divided by 30, as < 1/30 Class II objects may be misidentified as Class I YSOs due to an edge-on disk orientation (Gutermuth et al. 2009). Internally coeval clouds like MonR2 and Ophiuchus appear to have very similar distributions for both YSO classes. In contrast, those that are more heterogeneous in their evolution have a clear systematic trend whereby there is an excess in the Class I distribution where the calibration value is low (gas-rich or YSO-poor) and an excess in the Class II distribution where the calibration value is high (gas-poor or YSO-rich).

Empirically, we define $\Sigma_*/\Sigma_{gas}^2 = 3 \times 10^{-4}$ and 5×10^{-3} pc^2 M$_\odot^{-1}$ as boundaries that bracket the distributions of those clouds with clear correlations and set apart the extrema of local evolution that appear commonly in the more heterogeneous clouds. Note that we have reduced over three orders of magnitude variation in Σ_* to an approximately one order of magnitude variation in Σ_*/Σ_{gas}^2. $\Sigma_*/\Sigma_{gas}^2 < 3 \times 10^{-4}$ indicates a relative overdensity in gas, and the stars that are present there are predominatly of the younger type, Class I. We infer that the the onset of star formation was delayed in these regions, resulting in the presence of few YSOs and a large reservoir of molecular gas. On the other extreme, $\Sigma_*/\Sigma_{gas}^2 > 5 \times 10^{-3}$ suggests stellar overdensity relative to gas, and the stars found in this regime are nearly exclusively Class II YSOs. Thus we infer that these are regions where star-forming gas has been largely depleted by some combination of conversion into stellar mass or ejection of gas via radiative processes, such as photoevaporation, or winds from the recently formed stars. We summariuze the median Σ_*/Σ_{gas}^2 values by YSO class for each cloud in Table 3.

A majority of the YSO membership in each cloud (54%-85%) falls in the range of Σ_*/Σ_{gas}^2 between 3×10^{-4} and 5×10^{-3} pc^2 M$_\odot^{-1}$. This excludes regions of each cloud that have mostly dispersed their gas or appear to be just at the onset of star formation. Such a selection has been applied to make Figure 12, the Class II to Class I ratio of sources as a function of gas column density for each of the clouds. This analysis yields a diagnostic of the evolutionary state of the molecular clouds at different gas column densities. Even

within the restricted range of Σ_*/Σ_{gas}^2, there are significant variations in the ratio of Class II to Class I objects. Overall, most clouds show a trend of decreasing Class II to Class I ratio with increasing gas column density. This may suggest that the higher column density regions are younger than those with low column density.; however, there are several other possible interpretations for this trend. For example, the protostar phase may last longer in high density regions, or protostars in these regions may be less prone to oscillate between Class II and Class I SEDs (Dunham et al. 2010). Alternatively, the regions of low column density may be contaminated by Class II objects that have migrated from clusters. Gas dispersal may result in the high fraction of Class II at low gas densities; this may be especially important for the Cep OB3b, S140 and Perseus clouds. Finally, we cannot rule out observational biases. Although our adopted classification criteria were designed to minimize the influence of extinction, high extinction may result in the mis-classification of some Class II YSOs as Class I protostars.

4. Discussion

The Class II YSO evolutionary stage lasts between 0.5 and 5 Myr (Hernández et al. 2008), and the majority of the IR-excess sources included in this analysis are of that class. Therefore, the fact that the above power law trend is observed at all suggests a close link between the YSO spatial distribution and the gas structure on the timescale of ~2 Myr for the ~1 pc size scales probed here. While this is indeed a profound result, it is still in some sense unconstraining. The connection between the gas and the YSOs may in part result from the observed kinematic connection between dense cores and the surrounding molecular gas. Specifically, millimeter-line observations show that the the velocity dispersion between the cores and the surrounding, moderate density gas is small relative to the velocity dispersion inferred from the observed linewidth and the observed velocity gradients in the bulk gas motions (e.g. Walsh et al. 2004, 2007; Adams et al. 2006; Kirk et al. 2007; Jørgensen et al. 2008). However, the YSOs and their progenitor gas could simply co-move in aggregate around the larger structure of the cloud, perhaps even dynamically interacting with other such aggregations, and still pre-

serve the observed connection between the YSO and gas distribution. Thus, a dynamical picture for the cloud and the structures within the cloud is not ruled out by the star-gas correlation.

Under the simplifying assumption that there is relatively little motion between the YSOs or the gas, we present a simple model which adopts a star formation law where the star formation rate per area follows a power law of the local instantaneous gas surface densities. This model demonstrates that the likely gas depletion that has occured to generate the observed star-gas correlation still leaves behind a power law of similar index to the primordial relationship. We then establish that the observed star-gas correlations and the star formation law have a power law index ~2. Next, we demonstrate that simple thermal fragmentation of an isothermal, self-gravitating, modulated layer of gas can produce a spatial distribution of gravitationally unstable fragments where the surface density of fragments scales as the gas density squared. Finally, we briefly compare the reported star-gas correlation to similar recent analyses in the literature.

4.1. Comparing Star Formation Laws to the Σ_* vs. Σ_{gas} Relationship

As discussed in Section 1, several empirical star formation laws have been proposed in the literature; these laws relate the inferred star formation rate per area to the current column density of gas, and typically they are derived over large (>100 pc) size scale measurements. We examine here whether the observed ~1 pc scale Σ_* vs. Σ_{gas} correlation reported in Section 3 is consistent with a simple star formation law where the star formation rate per area varies linearly or as a power of the current gas column density.

In order to consider the likelihood that the reported power law correlation in observed quantities, ie. the integrated number of YSOs and the remaining amount of gas, relates at all to an underlying star formation law of power law form, we must consider whether the more efficient creation of stars at higher gas column density significantly affects the underlying gas distribution and therefore results in an observed Σ_* vs. Σ_{gas} distribution that deviates from the power law index of the star formation law itself. To this end, we present a simple model of gas to stellar mass conversion. Gas

mass is accreted onto stars at a rate governed by an assumed star formation law with an efficiency that accounts for the ejection of gas mass from the system via protostellar outflows.

The nature of this model demands several underlying assumptions to both achieve adequate simplicity and offer a relatively robust examination of how the observables behave with time. The first assumption is that the stars formed do not move significantly from their birth sites to within the typical resolution of our measurements ($\sim$1 pc scale). The observations that spatially proximate prestellar cores are likely formed with low relative velocities (Walsh et al. 2007; Muench et al. 2007) suggest that the typical velocity dispersion of of the YSOs that emerge from the cores is small ($\sim$0.4 km s^{-1}). Furthermore, later in the star formation process, relatively uniform surface density distributions are observed in many embedded YSO groupings (Gutermuth et al. 2009), suggesting relatively little dynamical evolution. The second assumption is that there is no molecular gas flowing into or within the molecular cloud at the $\sim$1 pc scale; gas is only ejected from the system by the formation of stars, or converted into stellar mass. This assumption is adopted for simplicity; it is demonstrably false at scales <1 pc, where systematic gas infall motions have been observed in cluster-forming clumps (e.g. Williams & Myers 1999; Walsh et al. 2006), and on larger scales, the global freefall time of a typical GMC is $\sim$5 Myr, though turbulent support likely inhibits global collapse to some degree. Finally, we assume that there is no effect on the gas distribution by large scale effects from phenomena such as feedback from nearby high mass stars, supernovae, or galactic motions. These processes only affect the cloud on longer timescales (>10 Myr) than we are considering, with the exception of high mass star feedback that we ignore for simplicity.

We begin by adopting a general star formation law where the star formation rate per area shows a power law dependence on the gas column density:

$$\frac{\partial \Sigma_\star(x,y,t)}{\partial t} = ck\Sigma_{gas}(x,y,t)^\alpha \qquad (1)$$

where $\Sigma_\star(x,y,t)$ is the mass surface density of YSOs as a function of position in the sky and time, k is a constant that is defined in equation 2 below, and $\Sigma_{gas}(x,y,t)$ is the mass column den-

sity of molecular gas as a function of position and time. We have assumed that the formation of a star depletes the cloud by $M_\star/c$ where $M_\star$ is the mass of the star created and c is the mass conversion efficiency which takes into account the mass of gas ejected from the cloud by feedback during star formation ($M_{ejected} = M_\star/c - M_\star$). Here we are assuming that the fraction of the mass in the outflow ejected from the cloud is constant throughout the cloud, but in fact the fraction of mass that escapes the cloud's gravitational potential may vary as a function of local gas column density and be affected further by the nearby gas configuration at >1 pc scales. Furthermore, it is worth noting that in this formulation we are not considering individual stars, thus the entire analysis, including the value of c, is averaged over the stellar initial mass function (IMF), regardless of its form. A prestellar core to star mass conversion efficiency that is constant over the stellar mass range is consistent with recent characterizations of the mass function of pre-stellar cores (e.g. Alves, Lombardi & Lada 2007; André et al. 2010). They find a value for this efficiency of 0.3 ± 0.1. However, this does not speak to the amount of unaccreted matter that is ejected from the cloud entirely; thus we consider 0.3 as a lower limit on the value of c.

If we assume that no additional gas is flowing into or within the cloud as the stars form, then the rate of depletion of the gas mass is given by:

$$\frac{\partial \Sigma_{gas}(x,y,t)}{\partial t} = -k\Sigma_{gas}(x,y,t)^\alpha \qquad (2)$$

In the case that $\alpha \neq 1$, the solution for $\Sigma_{gas}(x,y,t)$, the gas density remaining in the cloud, is:

$$\Sigma_{gas}(x,y,t) = \Sigma_{gas}(x,y,0)(\frac{t}{t_0} + 1)^\beta \qquad (3)$$

where, $\Sigma_{gas}(x,y,0)$ is the column density of gas at the onset of star formation, β is a constant, and t_0 is the timescale for the gas to be depleted by a factor of 2^β. Specifically:

$$\beta = \frac{1}{1-\alpha} \qquad (4)$$

and

$$t_0 = \frac{1}{k(\alpha-1)}\Sigma_{gas}(x,y,0)^{1-\alpha} \qquad (5)$$

8

Note that t_0 depends on the initial column density of gas for $\alpha > 1$; in this case regions with higher column densities will be depleted more rapidly. The amount of mass converted into stars is then the mass of the depleted gas times the mass conversion efficiency, c:

$$\Sigma_*(x,y,t) = c[\Sigma_{gas}(x,y,0) - \Sigma_{gas}(x,y,t)] \quad (6)$$

Substituting equation Eqn. 3 into Eqn 6, we obtain the relationship:

$$\Sigma_\star(x,y,t) = c\Sigma_{gas}(x,y,0)[1 - (\frac{t}{t_0} + 1)^\beta]. \quad (7)$$

In the case that $t << t_0$, we find that $\Sigma_\star(x,y,t)$ has the same power law dependence as the star formation rate:

$$\Sigma_\star(x,y,t) = c\Sigma_{gas}(x,y,0)^\alpha kt \quad (8)$$

In other words, the surface density of formed stars is proportional to the surface density of initial gas to the α power. In this limit, the observed gas density can be approximated as $\Sigma_{gas}(x,y,t) = \Sigma_{gas}(x,y,0)$ and the following approximation for the star formation rate can be used:

$$\frac{\partial \Sigma_\star(x,y,t)}{\partial t} = \frac{\Sigma_\star(x,y,t)}{t} = ck\Sigma_{gas}(x,y,t)^\alpha \quad (9)$$

In the case that the star formation rate is proportional to the gas density, i.e. $\alpha = 1$ (even though our data cannot be reproduced by such a law, as we next show), we have a different solution to equation 2 for the gas remaining, $\Sigma_{gas}(x,y,t)$:

$$\Sigma_{gas}(x,y,t) = \Sigma_{gas}(x,y,0)e^{-kt} \quad (10)$$

and for $\Sigma_\star(x,y,t)$ we find the solution:

$$\Sigma_\star(x,y,t) = c\Sigma_{gas}(x,y,0)[1 - e^{-kt}] \quad (11)$$

which becomes, in the limit of $kt << 1$:

$$\Sigma_\star(x,y,t) = c\Sigma_{gas}(x,y,0)kt \quad (12)$$

Eqn. 12 thus simplifies to Eqn. 8 for the $\alpha = 1$ case, under a similar assumption of small t.

At this point, we have argued that a power law observed in Σ_* vs. Σ_{gas} is indicative of a star formation law of similar functional form. Therefore, it is interesting to examine the $\alpha = 2$ case, as suggested by the analysis from Section 3.

Combining Eqn. 3 and 5 under the assumption that $\alpha = 2$ allows us to find a useful expression for the quantity $\Sigma_\star/\Sigma_{gas}^2$ computed in Section 3:

$$\frac{\Sigma_\star}{\Sigma_{gas}^2}(x,y,t) = ckt(1 + \frac{t}{t_0}) \quad (13)$$

Thus for $\alpha = 2$, the histograms presented in Fig. 11 can be thought of as histograms of normalized star counts for Class I and II YSOs vs. $ckt_{SF}(x,y)(1 + \frac{t_{SF}}{t_0}(x,y))$ at the current mean age of the YSOs at a given position, $t = t_{SF}$. Using this result and the observed evolutionary phase ratios of the YSO population, N_{II}/N_I vs. $\Sigma_{gas}(x,y,t_{SF})$ (Fig. 12), we can constrain the constant k and thus the gas depletion time $t_0(\Sigma_{gas})$. Then we can directly compare our data to the gas depletion model.

Here we measure $t_{SF}(x,y)$ by computing the ratio of the surface density of stars formed divided by the star formation rate surface density. We assume that the star formation rate surface density is constant in time and that it is approximated by the ratio of the surface density of Class I objects over the lifetime of that evolutionary phase, Σ_I/t_I, where $t_I \sim 0.5$ Myr (Evans et al. 2009). Thus:

$$t_{SF}(x,y) = \Sigma_*(x,y,t_{SF}) \times t_I/\Sigma_I(x,y) \quad (14)$$

$\Sigma_*(x,y,t_{SF}) = \Sigma_I(x,y) + \Sigma_{II}(x,y,t_{SF})$ in this analysis, thus we can simplify to:

$$t_{SF}(x,y) = (\frac{N_{II}(x,y,t_{SF})}{N_I(x,y)} + 1) \times t_I \quad (15)$$

As shown in section 3, we have computed N_{II}/N_I for each cloud as a function of gas column density, noting that some clouds have a downward trend, while others are fairly stable over the whole range of density values. The more extreme variations occur in clouds with wider spreads in Σ_*/Σ_{gas}^2, thus we assume that those clouds have some contamination of lower gas column density regions by older YSOs (via their motion away

from their birth sites) or that a large fraction of the primordial gas in those regions has been recently ejected by feedback from nearby, high mass stars. Given these complications, we have chosen to characterize the trend in N_{II}/N_I vs. Σ_{gas} from the relatively uniform MonR2 data, yielding:

$$\frac{N_{II}}{N_I}(x,y,t_{SF}) = 25 \times \Sigma_{gas}(x,y,t_{SF})^{-0.4} \quad (16)$$

The observed data are largely confined to the range $20 < \Sigma_{gas}(x,y,t_{SF}) < 300$ $M_\odot$ pc^{-2}; evaluating eqn. 16 at these fiducial points yields $N_{II}/N_I = 7.5$ and 3, respectively, and $t_{SF} = 4.3$ and 1.8 Myr, respectively. We now use these results to set limits on the value of k, and thus t_0.

Since t_{SF} and t_0 depend on quite different powers of Σ_{gas}, the case of $t_{SF} << t_0$ likely occurs at low initial gas column densities (this will be verified later), thus the higher value, $t_{SF} = 4.3$ Myr, is applicable. Assuming $c = 0.3$ (the lower limit), then $2.3 \times 10^{-4} < k < 3.9 \times 10^{-3}$ Myr^{-1} pc^2 $M_\odot^{-1}$. Therefore, at the corresponding value of Σ_{gas} (20 $M_\odot$ pc^{-2}), where the depletion time is long and thus $\Sigma_{gas}(x,y,t) = \Sigma_{gas}(x,y,0)$, we find that the depletion time is $13 > t_0 > 220$ Myr[3]. This range is 4 to 50 times larger than $t_{SF} = 4.3$ Myr and thus consistent with the $t_{SF} << t_0$ assumption. Assuming that the spread in the MonR2 Σ_*/Σ_{gas}^2 values are dominated by data uncertainty[4], we adopt the log-scaled mean value for the $\alpha = 2$ case, $k = 9.5 \times 10^{-4}$ Myr^{-1} pc^2 $M_\odot^{-1}$.

With k adopted, we now determine the gas column density where $t_0 = t_{SF}$, as this is the regime where significant gas depletion is expected in the data and thus where deviations from a power law star-gas correlation would be detectable. For $\alpha = 2$, t_0 is the time at which $\Sigma_{gas}(x,y,t_0) = 0.5\ \Sigma_{gas}(x,y,0)$. Therefore:

---

[3]Note that t_0 would increase (as k would decrease) linearly if c is larger, and $c \leq 1$ by its definition above.

[4]Our stellar surface densities are $n = 11$ nearest neighbor densities, which are inherently uncertain at the 33% level (Casertano & Hut 1985), and our gas surface densities are uncertain at 0.5-4 A_V, with higher uncertainty at higher surface densities. These uncertainty sources result in 1σ uncertainties of $\sim$0.3 dex in Σ_*/Σ_{gas}^2 values, thus they are sufficient to account for the ± 0.6 dex range in those values in MonR2, assuming that they are log-normally distributed and that our adopted limiting values isolate the central $\pm 2\sigma$ range.

$$t_0 = \frac{1}{2k}\Sigma_{gas}(x,y,t_0)^{-1} \quad (17)$$

Setting $t_0 = t_{SF}$ and thus this equation equal to Eqn. 15 and solving numerically, we find $\Sigma_{gas}(x,y,t_{SF} = t_0) = 300 M_\odot$ pc^{-2}. Thus gas depletion only becomes noticeably relevant at gas column densities on the high end of the observed range.

In summary, the model closely follows the observed power law correlation between star formation rate surface density and gas column density. Only at the highest observed column densities does the model predict significant deviations from a power law: these may be undetected due to the scatter in the observed correlation.

At this point, it is useful to visualize the time evolution of the simple gas depletion model and compare it with our observations. In Fig. 13, we plot the realizations of Equation 7 for several values of t in the range of 200 years to 6.3 Myr and a range of $\Sigma_{gas}(t = 0)$ from 20 to 2000 $M_\odot$ pc^{-2}, assuming $\alpha = 2$, $c = 0.5$, and $k = 9.5 \times 10^{-4}$ Myr^{-1} pc^2 $M_\odot^{-1}$. These realizations are isochrones showing the locus in the Σ_* vs. Σ_{gas} diagram for an ensemble of co-eval molecular cloud parcels with different initial values of Σ_{gas}. We also plot orthogonal tracks that trace the evolution in Σ_* vs. Σ_{gas} for parcels of a molecular cloud as the gas of a given $\Sigma_{gas}(t = 0)$ is converted into stars. The polygonal regions that demarcate the observed data limits for MonR2 (green) and Ophiuchus (blue) are overplotted for comparison. At early t, the model follows a power law of index $\sim$2. As we approach typical star formation region ages of $\sim$1 Myr, the highest gas density evolutionary tracks curve toward decreasing gas densities, resulting in local steepening of the model isochrone. This is a direct result of the varying relative rate of gas depletion at differing column densities. For the lowest initial gas densities, the evolutionary tracks follow an almost vertical trajectory as stars are formed at very low efficiency. In contrast, the higher initial gas densities form stars very efficiently and thus the gas is quickly depleted relative to the star formation time, t_{SF}. We can easily rewrite Eqn. 13 to describe the star formation efficiency at $t = t_{SF}$ as:

$$\frac{\Sigma_*}{\Sigma_* + \Sigma_{gas}}(x, y, t_{SF}) = \frac{\Sigma_{gas}(x, y, t_{SF})}{\Sigma_{gas}(x, y, t_{SF}) + 1/(ckt_{SF}(1 + \frac{t_{SF}}{t_0}))} \tag{18}$$

At the Σ_{gas} fiducial points of 20 and 300 $M_\odot$ pc^{-2} adopted above, $\frac{\Sigma_*}{\Sigma_* + \Sigma_{gas}}(x, y, t_{SF}) = 2.3\%$ and 26% respectively. These are similar to reported values for "distributed" and "clustered" star formation (e.g. Carpenter 2000; Allen et al. 2007; Evans et al. 2009). In this analysis, as is claimed by Bressert et al. (2010), we see a smooth variation from low to high column density star formation. We add to that analysis that the most likely progenitor of the smooth variation in stellar densities is the smooth variation of gas column densities in star forming clouds.

In Fig. 14, we investigate different values of α, as well as the possibility of a threshold in density for star formation, and compare the results to the fits to the MonR2 and Ophiuchus clouds. We show Equation 7 models for $\alpha = 1$ (top left panel) and $\alpha = 1.4$ (top right panel), with no threshold imposed, and with appropriate values of k (α-dependent) to approximately fit the MonR2 and Ophiuchus data (green and blue polygons, respectively): neither provides a good fit to the data, unlike that in Fig 13. We also implement a threshold (bottom two panels) such that the star formation ceases when $\Sigma_{gas}(x, y, t)$ is less than a value of 100 $M_\odot$ pc^{-2}. A less extreme threshold has been reported in a different analysis of the *Spitzer* c2d and Gould Belt Legacy survey data, where protostars alone are used to compute star formation surface densities (Heiderman et al. 2010). Our analysis is not consistent with a star formation threshold at any gas column density in the range that we have surveyed.

4.2. A Simple Model of Jeans Fragmentation

For MonR2 and Ophiuchus, the power law indices in the relation between stellar and gas surface density are close to 2. This section shows that such an exponent is expected from a simple model of Jeans fragmentation in an isothermal self-gravitating layer.

If one initial Jeans mass makes one star, then the number surface density of stars in a layer equals the number surface density of Jeans masses,

$$N_* = N_J \tag{19}$$

The Jeans mass in a self-gravitating layer is

$$M_J = \frac{B\sigma^4}{\Sigma_{gas} G^2} \tag{20}$$

where B is a constant (4.67 for an isothermal, self-gravitating layer of gas; Larson 1985), σ is the gas velocity dispersion, Σ_{gas} is the gas mass surface density, and G is the gravitational constant.

Then the number surface density of Jeans masses can also be written as

$$N_J = \frac{\Sigma_{gas}}{M_J} \tag{21}$$

or substituting from 20,

$$N_J = \frac{1}{B}\left(\frac{G\Sigma_{gas}}{\sigma^2}\right)^2 \tag{22}$$

and substituting from 19, multiplying both sides of the equation by a mean mass per star of 0.5 $M_\odot$[5], and converting to mass surface density units of $M_\odot$ pc^{-2}, with an assumed $\sigma = 0.2$ km s^{-1}, the sound speed at 10 K:

$$\Sigma_* = 1.34 \times 10^{-3} \Sigma_{gas}^2 \tag{23}$$

Thus the power law of index 2 is predicted by simple thermal fragmentation of an isothermal self-gravitating layer. Furthermore, the value of 1.34×10^{-3} is in the middle (in log-space) of our observed range of Σ_*/Σ_{gas}^2 from section 3, and represents a mean value for $ckt(1 + t_{SF}/t_0)$ in the evolutionary model above. We note that there is no explicit time dependence in this model, thus although it gives the correct star-gas correlation, it does not predict a rate of star formation.

More generally, one must consider cloud layers that are non-uniform, spanning a wide range of column densities in order to replicate the trends

---

[5]Note that the eventual mass of a given star is explicitly assumed to be uncorrelated with the local Jeans mass. This is consistent with some characterizations of the pre-stellar core to stellar mass conversion process that include potential accretion of gas from the larger-scale environmental distribution (e.g. Myers 2008, 2009b).

we report here, which are found within each star-forming cloud individually. An example of a horizontally nonuniform planar system is the density-modulated isothermal layer (Schmid-Burgk 1967), or of a planar system of isothermal cylinders (Ostriker 1964) can be expected to give a similar relation between stellar and gas surface densities. Some of the clouds studied in this paper may have such a flattened geometry; their extinction maps indicate that "hub-filament" structure is expected if a clumpy medium is compressed into a modulated self-gravitating layer (Myers 2009a).

If this picture of fragmentation in a layer applies to some of the clouds considered here, the results of Section 4.1 indicate that evolutionary effects probably do not change the relation between star and gas surface density very much, over the likely star-forming life of the cloud.

4.3. Empirical Comparison to Cloud-Scale Values, the Kennicutt-Schmidt Law, and Recent Parsec-scale Work

As already noted, Evans et al. (2009) compared the *overall* star formation surface density vs. gas column density for each of the clouds in the c2d survey, as well as an average of all of them, for comparison with the Kennicutt-Schmidt law for galaxies. They find that the star formation rate density predicted by the law falls a factor of 20 below their observed data. In Figure 15, we have overlaid the correlation reported here for even smaller scales (0.3 to 2.0 pc) on our reproduction of the Evans et al. (2009) figure. Our correlation overlays the Evans et al. (2009) cloud-averaged data well at intermediate surface densities, and the mean value for all clouds falls quite close to our correlation. The difference is only clear where our trend extends to higher column densities. Because we are able to probe a wider range in gas column density by taking measurements at smaller size scales, it is not surprising that such a discrepancy could be uncovered. Regardless, our analysis agrees with that of Evans et al. (2009); studies of star formation rate density versus gas density for nearby clouds show much greater star formation rate for the local gas density than extragalactic correlations would suggest. As noted by Evans et al. (2009) and others, the measurements used to derive most star formation law characterizations vary widely in the size scales and time

scales probed, and these variations almost certainly play a role in the apparent discrepancies. Indeed, recent work to characterize the role of measurement size scale in characterizing the correlation between star formation rate surface densities and gas surface densities in nearby galaxies has revealed considerable change in the power law index with the measurement size scale used (Liu et al. 2011).

Other recent efforts have examined the star formation rate and gas surface density correlation in nearby star-formation regions via similar sorts of data (ie. YSO star counts and near-IR extinction maps) and some overlap in the specific clouds considered. Lada et al. (2010) estimated the star formation rate vs. cloud mass for a sample of 11 nearby clouds. Within this cloud sample, they noted that there was a wide dispersion in the estimated star formation rate per cloud mass. They then demonstrated that the observed dispersion within their cloud sample was minimized if they only considered the cloud mass at column densities above $A_V = 7$ (or 116 $M_\odot$ pc^{-2}). They proposed that this corresponded to a density threshold for star formation; for densities above this threshold the star formation rate varied linearly with gas mass, below the threshold the star formation rate was negligible.

A similar threshold (129 ± 14 $M_\odot$ pc^{-2}) was invoked by the sub-cloud-scale analysis by Heiderman et al. (2010), a follow-up to the cloud-scale examination by Evans et al. (2009) mentioned above. Heiderman et al. (2010) used the numbers of *Spitzer*-identified Class I and so-called "flat spectrum" YSOs (ie. they excluded the longer-lived Class II YSOs) within various extinction contour intervals to probe the correlation in 20 nearby molecular clouds. Since their *Spitzer* data did not include clouds forming massive stars, they did not have a direct measurement of YSO densities in high mass star forming regions. Thus they added star formation rates derived from *IRAS* far-IR luminosities and mean gas column densities derived from HCN line emission for a set of more distant and presumably more active star-forming regions. We have overlaid their final bent power law best fit to their combined data in Fig. 15 (red solid lines), showing that it underestimates the star formation rates we report here at both extremely high and low gas column

densities.

At high column densities, the shallow portion of the bent power law of Heiderman et al. (2010) is driven by the inclusion of the *IRAS*-HCN-derived data in the fit; their *Spitzer*-derived data seem relatively consistent with our analysis (examined in more detail below). That work includes a discussion of the likelihood that far-IR-derived star formation rates may be underestimated for individual star-forming regions by up to an order of magnitude. We find plenty of evidence for that to be the case in the nearby embedded clusters, where we can do direct comparisons between the *IRAS* far-IR-derived star formation rate and that derived from the YSO counts. For example, using the known far-IR luminosity (26,000 $L_\odot$; Ridge et al. 2003) and the YSO count for the cluster core of the MonR2 main cloud core (132 YSOs, 0.73 pc effective radius; Gutermuth et al. 2009), we obtain star formation rate surface densities of 3 and 20 $M_\odot$ yr^{-1} kpc^{-2}, respectively. A similar discrepancy can be found in the Orion Nebula Cluster. Its far-IR luminosity is estimated at 10^5 $L_\odot$ (Gezari et al. 1998), yet its central parsec contains of order 10^3 YSOs (e.g. Feigelson et al. 2005), yielding SFR surface density estimates of 20 and 300 $M_\odot$ yr^{-1} kpc^{-2}, respectively. In summary, the common conversion of far-IR flux to star formation rate appears to underestimate the true star-formation rate at parsec scales in nearby regions.

We are not concerned with the apparent discrepancy with our result at low gas column densities. The protostellar number counts (Heiderman et al. 2010) at these gas column densities are very low: a star surface density of $10^{-1.7}$ $M_\odot$ kpc^{-2} yr^{-1} corresponds to one 0.5 $M_\odot$ protostar per 0.5 Myr (the estimated lifetime of the evolutionary phase) in the area of an entire typical molecular cloud ($\sim$ 10 pc size scale is typical of nearby clouds). We used the fitting technique described in Section 3 to fit their *Spitzer*-derived data, excluding the upper limits. We find that the *Spitzer*-only correlation to be a power law of slope 3.7 ± 1.6 (dashed red line in Fig. 15), a steeper power law than our reported trend (though within 1σ) and lacking in an apparent gas surface density threshold for star formation. Differences at this level may be explained in part by differences in source classification method and uncer-

tainty in the relative durations of the pertinent YSO evolutionary stages, but detailed consideration of such effects is beyond the scope of this paper.

5. Summary

We have presented an analysis of YSO and gas surface density at 0.3 to 2.0 pc scales for over 7000 YSOs in eight nearby molecular clouds from 40 square degrees of *Spitzer*- and 2MASS–surveyed sky. These plots show the relationship between the surface density of stars formed over the lifetime of the molecular cloud vs. the surface density of the remaining gas in the clouds. A power law correlation between these two quantities is evident in all eight molecular clouds included in the study. In summary:

- MonR2 and Ophiuchus have particularly strong and well-defined correlations, thus we fit them each with power laws (indexes of 2.67 and 1.87, respectively).

- Some clouds exhibit large deviations from the power law form apparent in MonR2 and Ophiuchus; we argue that these deviations are due to gas dispersal by massive stars and non-coevality in each cloud. The presence of non-coeval regions in the clouds is demonstrated by variations in the ratio of the numbers of Class II to Class I YSOs.

- Even given non-coevality and gas dispersal in most clouds, we find that greater than half of all YSOs with excess infrared emission in every cloud considered are found to have local Σ_*/Σ_{gas}^2 in the range of 3×10^{-4} and 5×10^{-3} pc^2 M$_\odot^{-1}$.

- Extracting the regions of each cloud found within a common evolutionary state ($3 \times 10^{-4} < \Sigma_*/\Sigma_{gas}^2 < 5 \times 10^{-3}$), the Class II to Class I ratio is shown to decline with gas column density. However, the magnitude of the decline varies by cloud, from near-uniform ratios with small declines in MonR2 and North America Nebula to steep declines in S140 and Perseus.

- The correlation can be reproduced by a simple model where the star formation rate per

13

unit area varies with the square of the surface density of gas. This model accounts for the gas removed from the cloud by the accretion and ejection of gas mass by each star. We find that the accretion and ejection of gas will cause deviation from the power law form, but will only result in a mild steepening of the correlation at high gas surface densities over the likely star formation timescales of a few Myr. In contrast, we find star formation laws where the star formation rate per area varies linearly or with the 1.4 power of the gas surface density are not able to fit the observed correlation.

- The observed dependence of the stellar surface density with the gas density squared is a prediction of the thermal fragmentation of a sheet-like isothermal layer. To achieve the observed range of local column densities, one must invoke some sort of nonuniformity in the local column density structure of the sheet, such as a "hub-filament" geometry as described and analytically characterized by Myers (2009a).

- The correlation reported here is largely consistent with recent *Spitzer*-derived estimates of star formation rate and gas surface densities both averaged over clouds (Evans et al. 2009) and measured within them (Heiderman et al. 2010). We have identified some systematic effects that may explain differences between our results and the analysis of Heiderman et al. (2010) that probes comparable size scales. Regardless of these differences, all of the work considered consistently suggests that extragalactic star formation rate and gas surface density correlations significantly underestimate those seen in nearby clouds.

A. Expansion of the c2d Extinction Maps

The c2d extinction maps are generated using extinction measurements from each source classified as having photospheric colors in their merged 2MASS and *Spitzer* catalogs. The measurement is a parameter returned as part of a blackbody fit to the 1-8μm spectral energy distributions of those sources, limited by what detections where achieved to reasonable S/N in that range. Unfortunately, that means that the c2d extinction maps are limited to the field of view at least covered by IRAC. Since the c2d survey areas were chosen to match elevated extinction in the surveyed clouds ($A_V > 3$), obtaining an unbiased local baseline is impossible from the maps directly. This baseline is needed to remove the foreground extinction to the reddening map.

In order to obtain a reasonable baseline A_V offset for the clouds surveyed by c2d, we had to expand those maps such that they extend beyond the IRAC-surveyed region, which was largely constrained to $A_V > 3$ areas in each cloud. Our process is as follows:

- Construct an A_V map of a large area around each cloud using the technique from Gutermuth et al. (2009) that was used for the non-c2d clouds included in this work.

- Resample the large map onto the c2d map's grid.

- Fit the $A_V(c2d)$ vs. $A_V(G09)$ correlation between the two maps using those pixels that have valid data in both maps, in the range where both maps should have strong agreement: $2 < A_V(c2d) < 10$.

- Convert the large map's A_V values to use the c2d map's effective reddening law and zero-point calibration using the fitted parameters and fill in the empty parts of the c2d map's grid.

The fits are shown in Figs. 16, 17, & 18, and the results are summarized in Table 4. The figures reveal a consistent deviation and spreading in the data for $A_V(c2d) > 12$ where the $A_V(c2d)$ values are generally higher than the fit. The declining background star density with increasing extinction forces the adaptive smoothing of the G09 method to smooth over poorly sampled high column density structure, diluting it in favor of higher statistical S/N. In addition, the inclusion of the IRAC-derived data in the c2d maps likely enables higher S/N extinction measurements in greater numbers in intermediate extinction regions.

The fit results are summarized in Table 4. The inclusion of IRAC data in the c2d extinction measurement process could lead to deviations in the effective reddening law; indeed, color excess ratios in various combinations of IRAC and 2MASS bandpasses have been shown to vary slightly (e.g. Serpens and Ophiuchus; Flaherty et al. 2007). That said, these effects are expected to be small, and that is born out by the $< 15\%$ variation indicated by the near-unity slopes of the fits. The offset calibration deviations are easily explained by the use of local reference fields in the c2d maps to establish the typical colors of field stars near each cloud. In constrast, the G09 technique adopts an intrinsic $H - K = 0.2$ color for field stars and then utilizes constant baseline subtraction away from the cloud to account for local variations. With our cross calibration, we ensure a fair baseline treatment for the c2d clouds, regardless of the differences in their construction.

Additionally, we can test how the extinction mapping technique affects the $\log \Sigma_*$ vs. $\log \Sigma_{gas}$ fit to the Ophiuchus cloud; the power law index is 1.93 ± 0.03 with reduced χ^2 of 5.01 using the map generated by our technique, and 1.87 ± 0.03 with reduced χ^2 of 4.78 using the c2d map. Thus the values differ by less than 10% and are within 1.5 sigma of each other.

Facilities: Spitzer.

REFERENCES

Adams, F. C., Proszkow, E. M., Fatuzzo, M., & Myers, P. C. 2006, ApJ, 641, 504

Allen, L., et al. 2007, Protostars and Planets V, 361

Allen, T. S., et al. 2011, in prep.

Alves, J., Lombardi, M., & Lada, C. J. 2007, A&A, 462, L17

André, P., et al. 2010, A&A, 518, L102

Baraffe, I., Chabrier, G., Allard, F., & Hauschildt, P. H. 1998, A&A, 337, 403

Bate, M. & Bonnell, I., 2005, MNRAS, 356, 1201

Bigiel, F., Leroy, A., Walter, F., Brinks, E., de Blok, W. J. G., Madore, B., & Thornley, M. D. 2008, AJ, 136, 2846

Bressert, E., Bastian, N., Gutermuth, R., et al. 2010, in review

Carpenter, J. M. 2000, AJ, 120, 3139

Casertano, S., & Hut, P. 1985, ApJ, 298, 80

Chavarría, L. A., Allen, L. E., Hora, J. L., Brunt, C. M., & Fazio, G. G. 2008, ApJ, 682, 445

Chen, J.-H. et al., 2009, ApJ, 705, 1160

Dunham, M. M., Evans, N. J., Terebey, S., Dullemond, C. P., & Young, C. H. 2010, ApJ, 710, 470

Dzib, S., Loinard, L., Mioduszewski, A. J., Boden, A. F., Rodriguez, L. F., & Torres, R. M. 2010, arXiv:1003.5900

Enoch, M. L., et al. 2006, ApJ, 638, 293

Enoch, M. L., Evans, N. J., II, Sargent, A. I., Glenn, J., Rosolowsky, E., & Myers, P. 2008, ApJ, 684, 1240

Evans, N. J., et al. 2009, ApJS, 181, 321

Feigelson, E. D., et al. 2005, ApJS, 160, 379

Flaherty, K. M., Pipher, J. L., Megeath, S. T., Winston, E. M., Gutermuth, R. A., Muzerolle, J., Allen, L. E., & Fazio, G. G. 2007, ApJ, 663, 1069

Getman, K. V., Feigelson, E. D., Luhman, K. L., Sicilia-Aguilar, A., Wang, J., & Garmire, G. P. 2009, ApJ, 699, 1454

Gezari, D. Y., Backman, D. E., & Werner, M. W. 1998, ApJ, 509, 283

Guieu, S., et al. 2009, ApJ, 697, 787

Gutermuth, R. A., Megeath, S. T., Muzerolle, J., Allen, L. E., Pipher, J. L., Myers, P. C., & Fazio, G. G. 2004, ApJS, 154, 374

Gutermuth, R. A., Megeath, S. T., Pipher, J. L., Williams, J. P., Allen, L. E., Myers, P. C., & Raines, S. N. 2005, ApJ, 632, 397

Gutermuth, R. A., et al. 2008, ApJ, 674, 336

Gutermuth, R. A., Megeath, S. T., Myers, P. C., Allen, L. E., Pipher, J. L., & Fazio, G. G. 2009, ApJS, 184, 18

Gutermuth, R. A., et al. 2011, in prep.

Harvey, P. M., et al. 2006, ApJ, 644, 307

Harvey, P., Merín, B., Huard, T. L., Rebull, L. M., Chapman, N., Evans, N. J., II, & Myers, P. C. 2007, ApJ, 663, 1149

Herbig, G. H. 1962, Advances in Astronomy and Astrophysics, 1, 47

Hernández, J., et al. 2008, ApJ, 686, 1195

Heiderman, A., Evans, N. J., II, Allen, L. E., Huard, T., & Heyer, M. 2010, arXiv:1009.1621

Hirota, T., et al. 2008, PASJ, 60, 961

Jørgensen, J. K., et al. 2006, ApJ, 645, 1246

Jørgensen, J. K., Johnstone, D., Kirk, H., Myers, P. C., Allen, L. E., & Shirley, Y. L. 2008, ApJ, 683, 822

Kennicutt, R. C. Jr. et al., 1998, ApJ498, 541

Kirk, H., Johnstone, D., & Tafalla, M., 2007, ApJ, 668, 1042

Koenig, X. P., Allen, L. E., Gutermuth, R. A., Hora, J. L., Brunt, C. M., 2008, & Muzerolle, J., ApJ, 688, 1142

Krumholz, M. R., & Tan, J.C, 2007, ApJ, 654, 304

Lada, C. J. 1987, IAU Symp. 115: Star Forming Regions (Dordrecht: Kluwer)

Lada, E. A., Depoy, D. L., Evans, N. J., II, & Gatley, I. 1991, ApJ, 371, 171

Lada, C. J. & Lada, E. A., 2003, ARA&A, 41, 57

Lada, C. J., et al. 2006, AJ, 131, 1574

Lada, C. J., Lombardi, M., & Alves, J. F. 2010, arXiv:1009.2985

Larson, R. B. 1985, MNRAS, 214, 379

Li, W., Evans, N. J., II, & Lada, E. A. 1997, ApJ, 488, 277

Liu, G., Koda, J., Calzetti, D., Fukuhara, M., & Momose, R. 2011, arXiv:1104.4122

Megeath, S. T., et al. 2004, ApJS, 154, 367

Megeath, S. T., et al. 2011, in prep.

Menten, K. M., Reid, M. J., Forbrich, J., & Brunthaler, A. 2007, A&A, 474, 515

Moscadelli, L., Reid, M. J., Menten, K. M., Brunthaler, A., Zheng, X. W., & Xu, Y. 2009, ApJ, 693, 406

Muench, A. A., Lada, C. J., Luhman, K. L., Muzerolle, J., & Young, E. 2007, AJ, 134, 411

Muench, A. A., Lada, C. J., Rathborne, J. M., Alves, J. F., & Lombardi, M. 2007, ApJ, 671, 1820

Myers, P. C. 2008, ApJ, 687, 340

Myers, P. C. 2009a, ApJ, 700, 1609

Myers, P. C. 2009b, ApJ, 706, 1341

Ostriker, J. 1964, ApJ, 140, 1056

Padgett, D. L. et al., 2006 ApJ, 645, 1283

Porras, A., Christopher, M., Allen, L., Di Francesco, J., Megeath, S. T., & Myers, P. C. 2003, AJ, 126, 1916

Press, W. H., Teukolsky, S. A., Vetterling, W. T., & Flannery, B. P. 1992, Numerical Recipes in C: The Art of Scientic Computing (Cambridge: Cambridge Univ. Press)

Rebull, L. M., et al. 2010, ApJS, 186, 259

Rebull, L. M., et al. 2011, ApJS, 193, 25

Ridge, N. A., Wilson, T. L., Megeath, S. T., Allen, L. E., & Myers, P. C. 2003, AJ, 126, 286

Rieke, G. H., & Lebofsky, M. J. 1985, ApJ, 288, 618

Román-Zúñiga, C. G., Elston, R., Ferreira, B., & Lada, E. A. 2008, ApJ, 672, 861

Schmid-Burgk, J. 1967, ApJ, 149, 727

Schmidt, M. 1959, ApJ, 129, 243

Spezzi, L., et al. 2008, ApJ680, 1295

Strom, K. M., Strom, S. E., & Merrill, K. M. 1993, ApJ, 412, 233

Teixeira, P. S. et al., 2006, ApJ636, 45

Walsh, A. J., Myers, P. C., & Burton, M. G. 2004, ApJ, 614, 194

Walsh, A. J., Bourke, T. L., & Myers, P. C. 2006, ApJ, 637, 860

Walsh, A. J., Myers, P. C., Di Francesco, J., Mohanty, S., Bourke, T. L., Gutermuth, R., & Wilner, D. 2007, ApJ, 655, 958

Wilking, B. A., Meyer, M. R., Robinson, J. G., & Greene, T. P. 2005, AJ, 130, 1733

Williams, J. P., & Myers, P. C. 1999, ApJ, 511, 208

Winston, E., et al. 2010, AJ, 140, 266

Wu, J., Evans, N. J., II, Gao, Y., Solomon, P. M., Shirley, Y. L., & Vanden Bout, P. A. 2005, ApJ, 635, L173

TABLE 1

DATA AND DERIVED PROPERTIES BY CLOUD

Name	Mass[a] ($M_\odot$)	Area (pc^2)	Resolution (pc)	Baseline A_V	Mean A_V[a]	Max. A_V[a]	N_{II}	N_I	Dist. (pc)	Dist. Ref.	YSO Ref.
MonR2	25800	1170.0	0.95	-0.5	1.5	17.1	815	188	830	1	9
CepOB3	16100	551.0	0.42	0.9	1.9	21.6	1976	196	700	2	9
S140	7150	200.0	0.51	0.8	2.4	21.3	470	56	750	3	9
Orion	33200	572.0	0.75	-1.0	3.9	24.1	2861	502	414	4	10
NANeb	24400	548.0	0.29	1.1	3.0	22.0	745	425	600	5	5
Oph	3070	43.0	0.20	0.2	4.8	38.0	179	71	150	6	11[b]
Perseus	4300	72.8	0.29	0.7	3.9	31.5	243	111	250	7	11[b]
Serpens	2590	45.0	0.48	3.7	3.8	18.7	141	54	415	8	11[b]

References. — (1) Carpenter (2000); (2) Moscadelli et al. (2009); (3) Hirota et al. (2008b); (4) Menten et al. (2007); (5) Rebull et al. (2011); (6) Wilking et al. (2005); (7) Enoch et al. (2006); (8) Dzib et al. (2010); (9) Gutermuth et al. (in prep.); (10) Megeath et al. (in prep.); (11) Evans et al. (2009)

[a]Integrated mass and mean and maximum A_V values are derived from the baseline-subtracted extinction maps for the areas within the *Spitzer* coverage.

[b]Minor source count discrepancies between our reported counts and Table 5 of Evans et al. (2009) have been confirmed by the authors as a mistake in their table. Under the their advisement, we have included counts derived from the source catalogs of Evans et al. (2009), and their Table 5 source counts summary will be corrected in a forthcoming paper on all of the Gould Belt clouds (M. Dunham, private communication).

TABLE 2

LOG Σ_* VS. LOG Σ_{gas} FIT COEFFICIENTS

Name	Pearson Index	Calibration Offset	Power Law Index	Reduced χ^2
MonR2	0.87	-4.42	2.67 ± 0.02	6.22
CepOB3	0.17	-2.21	1.77 ± 0.01	20.3
S140	0.52	-1.84	1.37 ± 0.03	7.81
Orion	0.60	-2.40	1.80 ± 0.01	17.9
NANeb	0.67	-3.54	2.15 ± 0.02	12.2
Ophiuchus	0.83	-3.10	1.87 ± 0.03	4.78
Perseus	0.59	-7.0	3.8 ± 0.1	13.0
Serpens	0.83	-3.05	1.95	[a]

[a]The Serpens fit's χ^2 minimization did not converge using the Flaherty et al. (2007) fitting technique; a simpler, unweighted bisector fit has been used to obtain the reported coefficients. Saturation in the gas column density appears to cause a dual valued signal in the high column density region of the trend.

TABLE 3

Σ_*/Σ^2_{gas} MEDIAN VALUES BY YSO CLASS

Name	Class II	Class I
MonR2	0.86×10^{-3}	0.68×10^{-3}
CepOB3	3.0×10^{-3}	1.0×10^{-3}
S140	1.7×10^{-3}	1.2×10^{-3}
Orion	1.7×10^{-3}	1.0×10^{-3}
NANeb	0.64×10^{-3}	0.81×10^{-3}
Ophiuchus	0.47×10^{-3}	0.40×10^{-3}
Perseus	1.9×10^{-3}	0.90×10^{-3}
Serpens	0.76×10^{-3}	0.57×10^{-3}

TABLE 4

EXTINCTION COMPARISON FIT COEFFICIENTS

| Name	Constant Offset (A_V)	Slope
Oph	0.666	0.959 ± 0.001
Perseus	1.127	1.126 ± 0.004
Serpens	1.633	0.922 ± 0.005
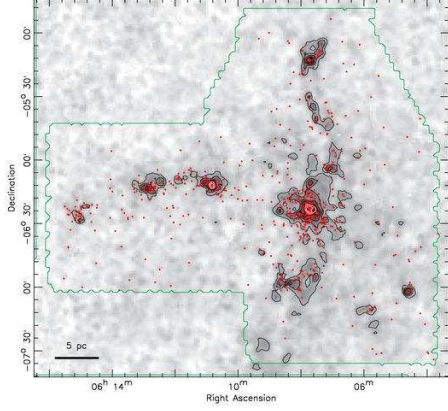
Fig. 1.— Extinction map of the MonR2 cloud overlaid in red with the spatial distribution of *Spitzer*-identified YSOs. The inverted grayscale is a linear stretch from $A_V = -1$ to 10 magnitudes. Contour overlays start at $A_V = 3$ mag and their interval is 2 mag. The IRAC coverage is marked by the green boundary. The projected positions of the YSOs in MonR2 closely trace almost all of the areas of detectably elevated extinction. Denser clusters of YSOs are clearly apparent in the zones of highest extinction.
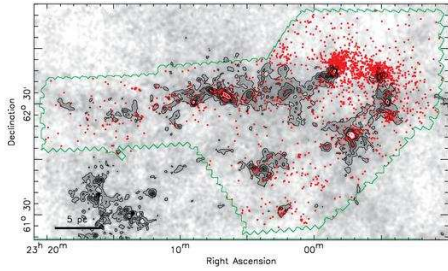
Fig. 2.— Extinction map of the CepOB3 cloud overlaid in red with the spatial distribution of *Spitzer*-identified YSOs. The grayscal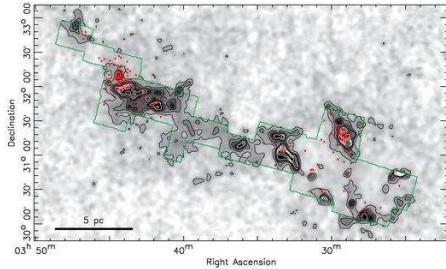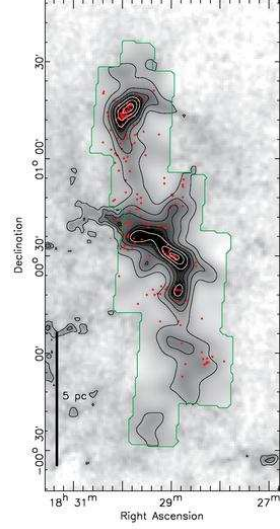e and contour properties are identical to those in Fig. 1. As in that figure, YSOs are predominantly projected on the elevated extinction zones within the cloud, and clusters are found in the highest extinction zones. However, unlike MonR2, the large CepOB3b young cluster in the northwest corner of the coverage is largely offset from significant extinction. Focussed examination of this region in particular suggests that the OB stars present have dispersed much of the local natal cloud material (Getman et al. 2009; Allen et al. in prep.).
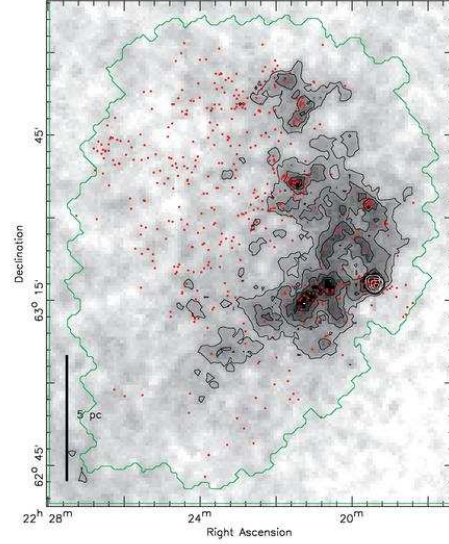
Fig. 3.— Extinction map of the S140 cloud overlaid in red with the spatial distribution of *Spitzer*-identified YSOs. The grayscale and contour properties are identical to those in Fig. 1.
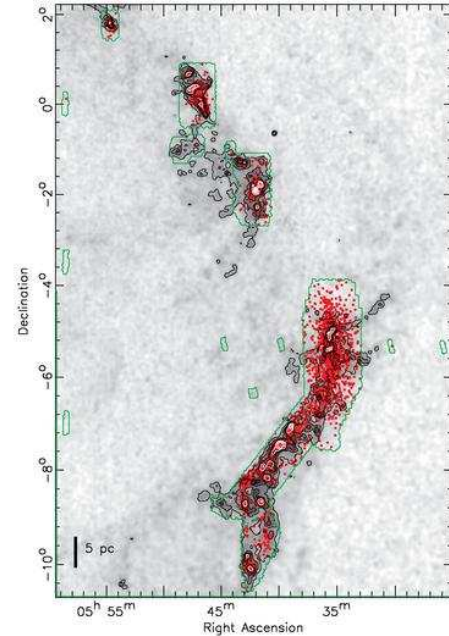

Fig. 4.— Extinction map of the Orion cloud overlaid in red with the spatial distribution of *Spitzer*-identified YSOs. The grayscale and contour properties are identical to those in Fig. 1.
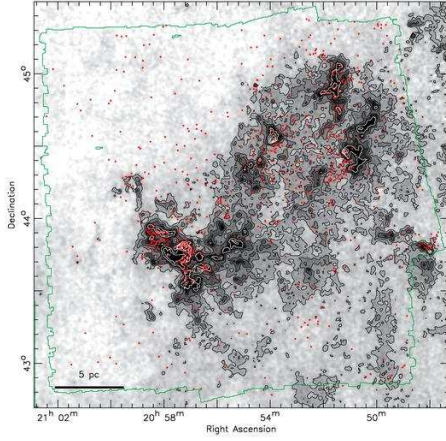
Fig. 5.— Extinction map of the NANeb cloud overlaid in red with the spatial distribution of *Spitzer*-identified YSOs. The grayscale and contour properties are identical to those in Fig. 1.
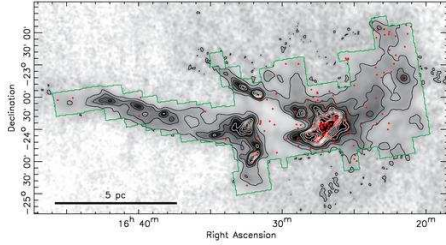
Fig. 6.— Extinction map of the Ophiuchus cloud overlaid in red with the spatial distribution of *Spitzer*-identified YSOs. The grayscale and contour properties are identical to those in Fig. 1.

Fig. 7.— Extinction map of the Perseus cloud overlaid in red with the spatial distribution of *Spitzer*-identified YSOs. The grayscale and contour properties are identical to those in Fig. 1.

Fig. 8.— Extinction map of the Serpens cloud overlaid in red with the spatial distribution of *Spitzer*-identified YSOs. The grayscale and contour properties are identical to those in Fig. 1.
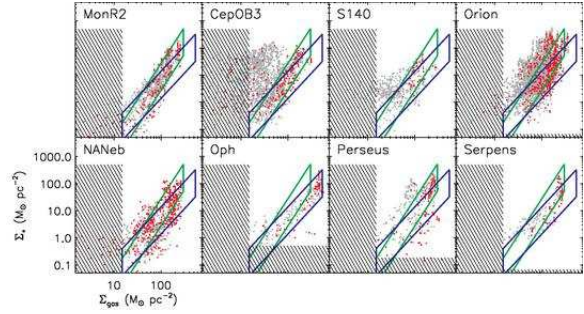
Fig. 9.— YSO surface density versus gas column density for the eight molecular clouds considered here. YSO surface density is computed from the local NN11 surface density of YSOs sampled at the position of each source. Gas column density is derived from the nearest sample to each YSO's position in the extinction map. Black hashed overlays mark out the regions of $A_V < 1$ (ie. consistent with zero, given typical uncertainties) and where the angular surface density of sources is less than 7 per square degree (consistent with residual contaminant sources according to the Gutermuth et al. (2009) classification scheme). The green polygon marks the fit to, and estimated spread in, the MonR2 cloud's data, and the blue polygon is the same, but for the Ophiuchus cloud's data.
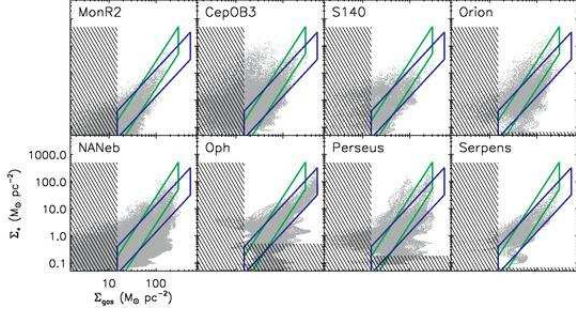
24

Fig. 10.— Same as in Fig. 9, but now the stellar surface densities are sampled uniformly by position on the same uniform grid as the extinction map instead of centered on the sources themselves. This area-sampled representation better represents regions of high gas column density but low YSO surface density.
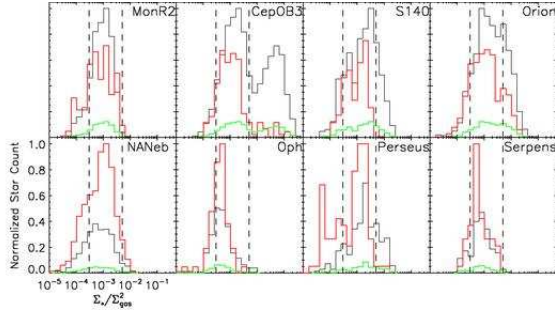

Fig. 11.— Histograms of Σ_*/Σ_{gas}^2 using the data in Fig. 9, separated by YSO evolutionary class. The Class II YSO histogram is in black, the Class I YSO histogram is in red, and each is normalized to their peak bin. The green histogram is the Class II histogram, but normalized to the Class I histogram's peak bin and then divided by 30. This represents the upper limit to the expected frequency that edge-on Class II sources will be misclassified as Class I YSOs (Gutermuth et al. 2009). Vertical dashed lines at $\Sigma_*/\Sigma_{gas}^2 = 3 \times 10^{-4}$ and 5×10^{-3} mark the empirical boundaries between different apparent evolutionary distinctions in the cloud: young, protostar-rich regions are on the left, most of the embedded cloud populations are found in the center and exposed, regions that have undergone gas dispersal are on the right.
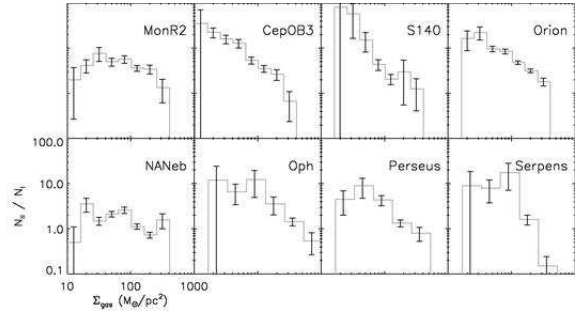

Fig. 12.— Class II to Class I source count ratio versus gas column density for those objects with $3 \times 10^{-4} < \Sigma_*/\Sigma_{gas}^2 < 5 \times 10^{-3}$. Among all clouds, there is a clear trend toward lower ratios at higher gas column densities. This could suggest that low gas column YSOs are relatively more evolved if they formed in situ (which could be suggestive of either an earlier onset of star formation in the currently low column zones or that the YSOs in high column zones have longer Class I phase lifetimes). Alternatively, the low column YSOs may have migrated from high density regions or may be the result of gas dispersal. This latter explanation may be particularly relevant for Cep OB3b, S140 and Perseus where there is clear evidence of gas dispersal.
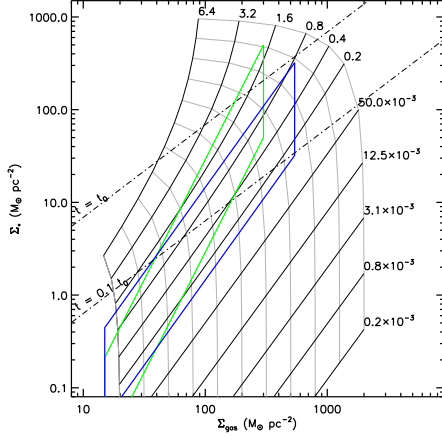
Fig. 13.— Results from the simple gas depletion model for an assumed star formation law of power law index 2 and an adopted star formation rate coefficient $k = 9.5 \times 10^{-4}$ Myr^{-1} pc^2 $M_\odot^{-1}$. Gray lines trace the star-forming evolution of parcels of gas of a given surface density through its evolution predicted by the model; as mass is converted from gas mass to stellar mass, the initial samples drift upward. For tracks that approach the regimes where $t \sim t_0$, gas is significantly depleted by the star formation process and points arc to the left as they rise. The black lines are isochrones defining the locus of points for the coeval evolution of molecular gas spanning a range of initial gas densities. The ages for each isochrone are noted, in Myr. The colored polygons demarcate the area that the observations of the MonR2 (green, steeper rise) and Ophiuchus (blue, shallower rise) clouds occupy. The dot-dashed lines mark where $t = t_0$ and $t = 0.1\ t_0$ for the model parameters chosen.
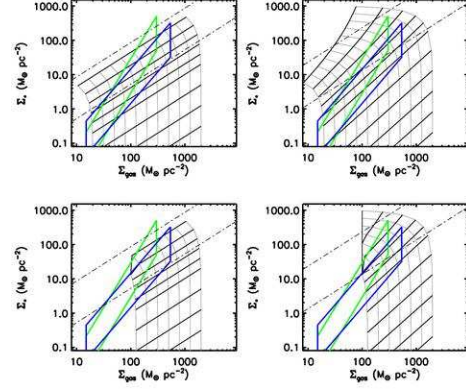

Fig. 14.— Several other realizations of the model; the left column assumes an initial power law of slope 1 and $k = 0.1$ Myr^{-1}, and the right column assumes a slope of 1.4 and $k = 0.05$ Myr^{-1} pc$^{0.8}$ $M_\odot^{-0.4}$; $c = 0.5$ in all realizations. These values of k were adopted to overlap with the observations, and do not affect the shape of the isochrones. The black isochrone lines are adopted for the same time steps as used in Fig. 13. The top row has no implicit gas column density threshold for star formation to occur. The bottom row includes such a threshold at 100 $M_\odot$ pc^{-2}; below that column density threshold, no stars are formed. The MonR2 and Ophiuchus data extent polygons (green and blue, respectively) and $t = t_0$ and $t = 0.1\ t_0$ dot-dashed lines are overplotted as in Fig. 13. The slope of 1 models are clearly inconsistent with the fits, and the slope of 1.4 with the star formation threshold is also inconsistent. The slope of 1.4 model with no threshold is consistent with the Ophiuchus fit if some degree of evolution is applied, as the approximate effect is a steepening of the trend with time.
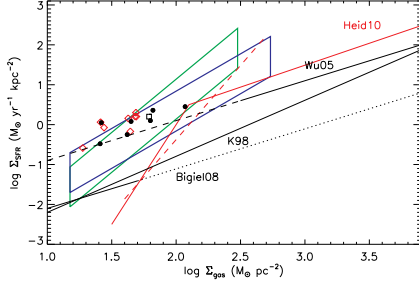
Fig. 15.— Our reproduction of the Star Formation Rate Surface Density vs. Gas Column Density figure from Evans et al. (2009). The filled black circles are mean measurements for entire molecular clouds from the c2d survey as presented in that work, and the open square is their mean. Red diamonds are similar cloud-integrated values derived from the data compiled in Table 1. The black lines are some recent correlations reported in the literature (Kennicutt et al. 1998; Wu et al. 2005; Bigiel et al. 2008) based largely on extra-galactic measures (500 pc or larger size scales). Dashed portions of the line are extrapolated relative to the reported range of each trend. The green and blue polygons demonstrating the correlations reported for MonR2 and Ophiuchus, respectively, have been converted to star formation rate density under identical assumptions to Evans et al. (2009) and overlaid. The cloud integrated values are consistent with our measurements, but the latter extend to higher column density because of the smaller size scales considered. The red trends are from Heiderman et al. (2010); the solid line is their bent power law fit to a combined set of *Spitzer*- and *IRAS*–derived data, and the dashed line is our fit to their *Spitzer*-derived data only.
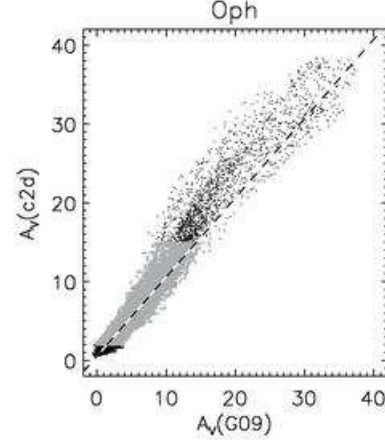

Fig. 16.— A_V comparison between the c2d-generated map of Ophiuchus and our own, resampled to their grid. The fit was performed on the gray points only, where we expect both maps to have strong agreement.
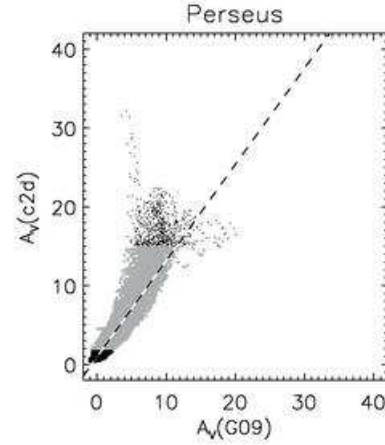

Fig. 17.— A_V comparison between the c2d-generated map of Perseus and our own, resampled to their grid. The fit was performed on the gray points only, where we expect both maps to have strong agreement.
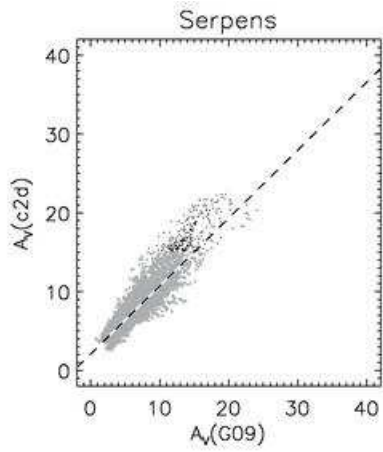
Fig. 18.— A_V comparison between the c2d-generated map of Serpens and our own, resampled to their grid. The fit was performed on the gray points only, where we expect both maps to have strong agreement.